Applied Physics B (2025) 131:58
https://doi.org/10.1007/s00340-025-08420-3

Applied Physics B
Lasers and Optics

RESEARCH

Design, fabrication, and characterization of dual-wavelength inhibited-coupling guiding hollow-core fibers

Bowen Chen[1,2] · Tim Kühlthau[1] · Götz Kleem[1] · Thomas Graf[1] · Marwan Abdou Ahmed[1]

Received: 17 December 2024 / Accepted: 11 February 2025 / Published online: 26 February 2025

Abstract

The present paper reports on the design, fabrication, and characterization of an 8-tube inhibited-coupling guiding hollow-core photonic crystal fiber (IC-HCPCF) capable of guiding both the beam emitted from an Yb:YAG laser at the fundamental wavelength of $\lambda = 1030$nm and its second harmonic at $\lambda = 515$nm. By controlling the strut thickness of the glass capillaries to approximately 362nm, the transmission of laser radiation at both wavelengths was possible with low losses. Optimizing the outer diameter of the glass capillaries mitigates the bending-induced increase of the confinement loss at the wavelength of 515nm without compromising the optical performance of the fiber at the wavelength of 1030nm. Experimental results confirm the near to diffraction-limited beam quality $\left(M^2 < 1.15\right)$ of the laser beams exiting the fiber at both operational wavelengths. Operating in the first transmission band at the wavelength of 1030nm, the calculated chromatic dispersion is $1.02\text{ps}/(\text{nm} \bullet \text{km})$, despite a diameter of the hollow core of 40μm. At the wavelength of 515nm this value amounts to $0.62\text{ps}/(\text{nm} \bullet \text{km})$. The measured losses are $27.5 \pm 0.3\text{dB}/\text{km}$ at the wavelength of 515 nm and $25.7 \pm 0.7\text{dB}/\text{km}$ at the wavelength of 1030 nm, which is comparable to the loss of state-of-the-art IC-HCPCFs with tubular cladding structures. The measured bending-induced increase of the confinement losses confirms the potential of the proposed approach for flexible, low-loss guiding of ultrashort laser pulses at the two wavelengths using a single fiber. This gained flexibility can significantly enhance the options for wavelength selection in laser material processing applications.

1 Introduction

The rapid progress in the development of ultrafast lasers, which typically emit at a wavelength of $\lambda = 1\mu$m, enabled numerous applications in industrial laser material processing. These applications include the drilling of micro-holes with a high aspect ratio [1], functionalizing material surfaces with periodic micro and nanostructures [2], and post-processing additively manufactured aluminum parts [3]. The better focusability of the frequency-doubled ultrafast laser radiation in the green spectral range offers opportunities for precise drilling of micro-holes with smaller structures and greater depths [4]. Drilling with frequency-doubled ultrafast lasers can minimize the influence of laser-induced atmospheric plasma and consequently enhance the process efficiency [5]. Moreover, the increased absorptivity (at room temperature) of copper with a value of approximately 40% at a wavelength of 515nm compared to the one of about 5% at a wavelength of 1030nm [6, 7] makes lasers emitting in the green spectral range advantageous for processing of copper or copper-based compounds in fields such as e-mobility [8], photovoltaics [9] and electrical power storage [10].

Inhibited-Coupling Guiding Hollow-Core Fibers (IC-HCPCFs) are capable of guiding light in a hollow air core with low losses [11], low dispersion [12], and offer single-mode guidance [13] thanks to their guiding mechanism based on the transverse mode mismatch between core-guided and cladding modes [14]. With a low power-weighted spatial overlap between the core-guided light with the surrounding silica strut on the order of 10^{-4} to 10^{-6} [15], IC-HCPCFs are considered as an ideal solution for the flexible delivery of ultrashort laser pulses with high peak intensities.

At the wavelength of $\lambda \approx 1\mu$m, the primary intrinsic loss mechanism in the IC-HCPCFs is the confinement loss [16]. This loss occurs because the core-guided modes in the hollow air core have a lower refractive index compared to the

✉ Bowen Chen
bowen.chen@ifsw.uni-stuttgart.de

[1] Institut für Strahlwerkzeuge (IFSW), University of Stuttgart, Pfaffenwaldring 43, 70569 Stuttgart, Germany

[2] Graduate School of Excellence Advanced Manufacturing Engineering (GSaME), University of Stuttgart, Nobelstraße 12, 70569 Stuttgart, Germany

one of the outer glass cladding, making these modes intrinsically leaky.

Various concepts of fiber claddings have been developed to improve the confinement of the core-guided light in the IC-HCPCFs within this near-infrared (NIR) spectral range. Improvements have been made to IC-HCPCFs with a Kagomé lattice cladding by incorporating hypocycloid core shapes. In 2018, Maurel et al. demonstrated a Kagomé IC-HCPCF with a low loss of 8.5 dB/km at $\lambda \approx 1030$nm [17]. In 2022, a 7-tube tubular IC-HCPCF was presented with a record low loss of 4.3dB/km at $\lambda \approx 1080$ nm [13]. Moreover, by introducing nested glass capillaries into the cladding structure of tubular IC-HCPCFs, the confinement losses of the hollow-core Nested Antiresonant Nodeless Fibers (HCNANFs) have been further reduced to 0.35 dB/km for a spectral range between $\lambda \approx 1023$ nm and $\lambda \approx 1100$nm [11].

The potential for guiding laser radiation in the green spectral range with low loss using IC-HCPCFs has also been explored with current state-of-the-art IC-HCPCFs facing limitations due to scattering losses at the rough glass-air interface [18]. During the fiber fabrication process, surface capillary waves (SCWs) can form on the surface of the molten silica glass and become frozen on the glass capillaries during solidification [19].

Several IC-HCPCFs have been developed to deliver beams from ultrafast lasers in the green spectral range with low losses. A Kagomé IC-HCPCF with a transmission loss of 150 dB/km at the wavelength of $\lambda \approx 515$ nm was first demonstrated in 2014 [20]. Two years later, a 6-tube IC-HCPCF with a core diameter of $26\mu m$ was fabricated. Despite the ultrabroad transmission band spanning over one octave, the measured losses were 80 dB/km at $\lambda \approx 532$ nm and more than 500 dB/km at $\lambda \approx 1064$ nm [21]. A 1 km long tubular IC-HCPCF with a core diameter of 42 μm surrounded by 9 glass capillaries exhibited a measured loss of about 13.8 dB/km at $\lambda \approx 539$ nm [22]. After successfully reducing the surface roughness at the glass-air interface using counter-directional gas and glass flows during the drawing process an 8-tube IC-HCPCF exhibited a new record low loss in the green spectral range of only 8.6 dB/km at $\lambda \approx 515$ nm [18].

Although the losses of IC-HCPCFs in the NIR and green spectral ranges have each been minimized, the potential for simultaneous guiding of radiation in both spectral ranges with low losses using a single IC-HCPCF remains unexplored. To date, there are still no existing single IC-HCPCFs capable of guiding ultrashort laser pulses at $\lambda = 515$ nm and at $\lambda = 1030$ nm with low losses. Therefore, the present work focuses on exploring the technological feasibility of guiding radiation with low losses in both spectral ranges using a single IC-HCPCF, while also aiming to initiate further scientific investigations. Typically, the transmission bandwidths with low losses of state-of-the-art IC-HCPCFs are limited to approximately $\Delta\lambda < 400$ nm [11]. Consequently, two main approaches are used for the delivery of ultrashort laser pulses in the green spectral range. The first involves directly guiding the frequency-doubled laser pulses at $\lambda = 515$ nm using IC-HCPCFs designed for the operation in the green spectral range [23]. The second is based on the frequency doubling of the ultrashort laser pulses at the fundamental wavelength of $\lambda = 1030$ nm only after transmission through IC-HCPCFs which are designed for the operation in the NIR spectral range [23]. The latter method requires good polarization-maintaining properties of the transport fiber. Both approaches, however, limit the degree of freedom for changes of the wavelength in a given system. In contrast, using a single IC-HCPCF that is capable to simultaneously deliver ultrashort laser pulses at both wavelengths allows for easy and fast switching between green and NIR radiation, thus enhancing the versatility of laser machines and opening up new applications in laser material processing. Moreover, in continuous-wave (cw) laser applications, deep-penetration welding of copper at $\lambda = 1030$ nm can be achieved by preheating the material with laser beams at $\lambda = 515$ nm [24]. Due to differing dominant loss mechanisms in the green and NIR spectral ranges, a thorough understanding of the optical behavior of IC-HCPCFs in both spectral ranges is essential.

The present study presents the design, fabrication, and characterization of an 8-tube IC-HCPCF, capable of guiding both the fundamental wavelength of an Yb:YAG laser at $\lambda = 1030$ nm and its second harmonic at $\lambda = 515$ nm. The balance between the mitigation of the bending-induced increase of the confinement loss at the wavelength of 515 nm and maintaining the optical performance of the fiber at the wavelength of 1030 nm was achieved by optimizing the outer diameter of the glass capillaries. The presented fiber was designed using the analytical expression for the critical bend radius in both spectral ranges [25] followed by a validation of the fiber design using finite-element method (FEM) modeling.

2 Fiber design

One distinguishing feature of IC-HCPCFs is the presence of spectral transmission windows with low confinement losses, which are separated by the resonant wavelengths where high confinement losses occur. The spectral positions of these resonant wavelengths can be approximated by [14]

$$\lambda_{resonant,l} = \frac{2T}{l}\sqrt{n_{glass}^2 - n_{air}^2}, \tag{1}$$

where T is the strut thickness of the glass capillaries, which is determined by the desired operation wavelength λ_{op}, l is an integer denoting the transmission band (1, 2, 3, …),

and n_{glass} and n_{air} are the refractive indices of glass and air, respectively. The bandwidth of the transmission window with low confinement losses, defined as the wavelength difference between two adjacent resonant wavelengths, can be expressed as

$$\Delta\lambda_{resonant,l} = \frac{2T}{(l-1)l}\sqrt{n_{glass}^2 - n_{air}^2} = \frac{\lambda_{resonant,l}}{(l-1)}. \quad (2)$$

In this context, we selected $\lambda_{op,NIR} = 1030$ nm for the fundamental wavelength of a Yb:YAG laser, and $\lambda_{op,Green} = 515$ nm for its second harmonic. For a given operational wavelength λ_{op}, the required thickness T of the strut can be calculated using [14]

$$T = \frac{(l-0.5)\lambda_{op}}{2\sqrt{n_{glass}^2 - n_{air}^2}}. \quad (3)$$

Choosing the appropriate thickness T is essential for guiding laser radiation in the green and NIR spectral ranges with low confinement losses using a single IC-HCPCF. To simultaneously guide laser radiation at the wavelengths of $\lambda_{op,Green} = 515$ nm and $\lambda_{op,NIR} = 1030$ nm within the same transmission band, only operation in the first transmission band is feasible, as indicated in Eq. (2). For $l \geq 2$, it is impossible to achieve low loss at $\lambda_{op,Green} = 515$ nm with $\lambda_{resonant,l} < 515$ nm while keeping $\Delta\lambda_{resonant,l} > 515$ nm to also cover the fundamental wavelength at 1030 nm. To guide laser radiation at both wavelengths within the first transmission band with low losses, where the bandwidth $\Delta\lambda_{resonant,1}$ is infinite towards longer wavelengths, it is sufficient to consider only the shorter operational wavelength $\lambda_{op} = \lambda_{op,Green}$ in Eq. (3). The thickness of the glass strut would then amount to $T = 121$ nm for $l = 1$ with $n_{glass} = 1.4615$ at $\lambda_{op,Green} = 515$ nm, presenting a significant challenge for the fabrication [26]. As the strut thickness of the glass capillaries T decreases, they become more susceptible to contact with each other in the neck-down region of the fiber preform during the drawing process [27]. Moreover, maintaining the uniformity in the cladding structure along the entire fiber length becomes more challenging due to the fluctuations in pressure or temperature in the furnace. To simplify the fabrication process and to improve the fiber's structural uniformity during fabrication, a glass strut thickness of $T = 362$ nm was chosen for $l = 2$ at $\lambda_{op,Green} = 515$ nm. This results in the first resonant wavelength $\lambda_{resonant,1} \approx 760$ nm, enabling the transmission of laser radiation at a wavelength of $\lambda_{op,NIR} = 1030$ nm in the first transmission band and the ones at a wavelength of $\lambda_{op,Green} = 515$ nm in the second transmission band of the fiber.

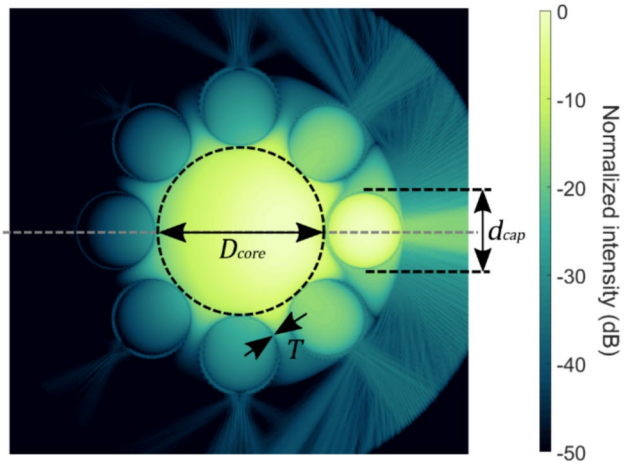

Fig. 1 Cross-sectional view of the computed normalized intensity distribution of the fundamental mode LP_{01} of a bent tubular IC-HCPCF with 8 glass capillaries at $\lambda_{op,Green} = 515$ nm. The dashed horizontal line marks the plane in which the fiber is bent towards the left with a radius of 0.12 m. The core diameter D_{core} is 40 μm and the outer diameter of the capillary d_{cap} is 18.5 μm with a strut thickness of $T = 362$ nm. Consequently, the optical power of the core-guided mode is coupled into the capillary on the right side which leads to a high bending-induced increase of the confinement losses. Note that for this fiber structure the critical bend radius at $\lambda_{op,Green} = 515$ nm is 0.12 m and therefore larger than the one of 0.03 m for $\lambda_{op,NIR} = 1030$ nm (not shown here)

One of the benefits of fiber-based beam delivery is its high flexibility. However, when an optical fiber is bent, the confinement losses increase exponentially as the bend radius diminishes. This fact is crucial in the design of IC-HCPCFs. For tubular IC-HCPCFs, the smallest acceptable bend radius is ultimately constrained by mode coupling between the core-guided fundamental mode LP_{01} and the fundamental mode guided in the cladding capillaries. As the bend radius decreases, the optical power from the core-guided mode leaks into the cladding glass capillaries, leading to significantly increased confinement losses. Figure 1 shows the normalized intensity distribution of the core-guided fundamental mode LP_{01} coupled with the fundamental mode of the cladding capillaries at a wavelength of $\lambda_{op,Green} = 515$ nm in an 8-tube IC-HCPCF.

The critical bend radius, below which the mode coupling occurs, can be analytically expressed by [25]

$$R_c = \frac{d_{cap} + D_{core}}{\left[\left(\frac{n_{eff,LP_{01}}}{n_{eff,cap,LP_{01}}}\right)^2 - 1\right]}, \quad (4)$$

where d_{cap} is the outer diameter of the glass capillary, D_{core} is the core diameter of the fiber (see Fig. 1), and $n_{eff,LP_{01}}$ and $n_{eff,cap,LP_{01}}$ are the effective refractive indices of the fundamental mode guided in the fiber's core and the glass capillaries, respectively [28]. The effective refractive index n_{eff}

of the fundamental modes guided in a IC-HCPCF's core and the cladding capillaries can be approximated by [28]

$$n_{eff} = n_{air} - \frac{1}{2}\left(\frac{x_{0,1}\lambda}{fD\pi}\right)^2 - \frac{x_{0,1}^2\lambda^3}{(fD)^3\pi^3}\frac{\left(n_{glass}^2+1\right)\cot\left(T\frac{2\pi}{\lambda}\sqrt{n_{glass}^2-n_{air}^2}\right)}{2\sqrt{n_{glass}^2-n_{air}^2}}, \quad (5)$$

where the constant $x_{0,1} \approx 2.405$ is the 1-st root of the Bessel function $J_0(x)$, D is the inner diameter of the considered core, hence D_{core} for the fiber or $d_{cap} - 2T$ for the glass capillary. The analytic expression for the effective refractive indices given here is only valid for a fiber consisting of a single glass capillary with perfectly circular core shapes surrounded by air [28]. As the shape of the core of IC-HCPCFs deviates from a perfect circle and the glass capillaries are in contact with the glass cladding of the fiber, a correction factor f is required to align the analytically calculated values from Eq. 5 to the numerically calculated ones. The correction factors are $f = 1.077$ for the fiber's core and $f = 0.991$ for the glass capillary in the cladding [29].

Figure 2 illustrates the relationship between the critical bend radius R_c and the ratio d_{cap}/D_{core}. It demonstrates that, for a given core diameter, reducing the ratio d_{cap}/D_{core} decreases the critical bend radius R_c. Moreover, for a given ratio value of d_{cap}/D_{core} and a given core diameter, the critical bend radius R_c at the wavelength of $\lambda_{op,Green} = 515$ nm is significantly larger than the one for $\lambda_{op,NIR} = 1030$ nm.

In applications of laser material processing, ultrashort laser pulses with high average and peak power are advantageous for many processes [1]. The primary limitation of fiber-based beam delivery systems for guiding such laser pulses

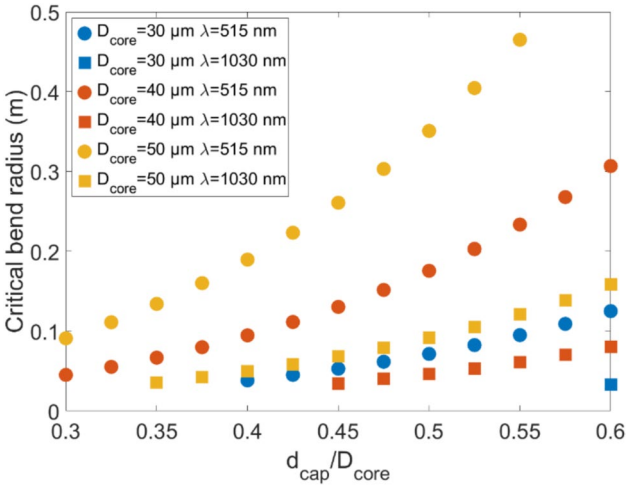

Fig. 2 Critical bend radius R_c of tubular IC-HCPCFs as a function of the ratio d_{cap}/D_{core} calculated using Eqs. (4) and (5) and assuming a strut thickness of $T = 362$ nm

is the laser-induced damage threshold (LIDT) [30], which depends on the power-weighted spatial overlap between the core-guided laser beam and the surrounding glass cladding. Increasing the diameter of the fiber's core D_{core} reduces this spatial overlap, thereby raising the LIDT of the fiber [31]. For a fiber with a core diameter as large as $D_{core} = 50\ \mu m$, however, a small ratio $d_{cap}/D_{core} < 0.3$ is necessary to keep the critical bend radius R_c at a value of less than 0.1 m. With such a small ratio d_{cap}/D_{core}, 10 glass capillaries are required to reduce the confinement losses for the straight fiber at $\lambda_{op,NIR} = 1030$ nm, which strongly increase the complexity of fiber fabrication. Considering these requirements, we selected a fiber design with a core diameter of 40 μm and a ratio of $d_{cap}/D_{core} = 0.375$. For tubular IC-HCPCFs with less than 8 capillaries, the gap between the glass capillaries at a ratio of $d_{cap}/D_{core} = 0.375$ results in high confinement losses of the straight fiber at $\lambda_{op,NIR} = 1030$ nm. Conversely, tubular IC-HCPCFs with more than 8 capillaries exhibit a minimal loss difference between the modes with higher transverse order and the fundamental mode LP_{01}, leading to the undesired effective multi-mode guiding property of the fiber. A cladding structure with 8 capillaries was therefore chosen for our fiber design. In the present work, the objective was to minimize the losses of the fiber in both spectral ranges to less than 30 dB/km and ensure a low bending-induced increase of the confinement losses for bend radii larger than 0.2 m. The target corresponds to a transmission of > 93.3% of the launched laser power through a 10 m long fiber, meeting the requirements for state-of-the-art delivery of ultrashort laser pulses in industrial applications.

To analyze the loss behavior of the designed tubular IC-HCPCF in detail, including the confinement losses, the surface scattering losses, and the micro-bending losses, we conducted numerical simulations based on FEM by using the commercially available software COMSOL Multiphysics.

The cross-sectional structure of the designed fiber was modeled using a MATLAB interface. To calculate the confinement losses of the modes propagating in the fiber's core, an optimized perfectly matched layer with a thickness of 10 μm was employed to absorb the radiation leaking out of the fiber's structure [32]. The maximum mesh size was set to be 0.2 times the wavelength to ensure a high accuracy of the calculated results. The confinement losses.

$$\alpha_{CL} = \frac{20}{\ln(10)}\frac{2\pi \cdot Im\left(n_{eff}\right)}{\lambda}\text{dB}. \quad (6)$$

were determined from the imaginary part $Im\left(n_{eff}\right)$ of the numerically calculated effective refractive indices of the core-guided modes [33]. The surface scattering losses α_{SSL} were also modeled numerically. First, the parameter

$$F = \sqrt{\frac{\varepsilon_0}{\mu_0}} \frac{\oint_{interface} \left|\vec{E}\right|^2 dl}{\iint \vec{E} \times \vec{H} dA \cdot \vec{z}}. \tag{7}$$

was calculated, where $\vec{E}$, $\vec{H}$ are the electric and magnetic fields, respectively, $\vec{z}$ is the unit vector in the propagation direction of the core-guided mode [19], and ε_0 and μ_0 are the permittivity and permeability in vacuum, respectively. The surface scattering losses at the wavelength λ of interest are then given by

$$\alpha_{SSL} = \eta F \left(\frac{\lambda}{\lambda_0}\right)^{-3} \frac{\text{dB}}{\text{km}}, \tag{8}$$

with the normalization factor $\eta = 300$ determined at the reference wavelength of $\lambda_0 = 1550$ nm, as shown in ref. [19].

Micro-bending of optical fibers can occur when the fiber is coiled onto a fiber drum with a rough surface under tension or during the cabling process with a bend radius on the order of μm to mm [16]. The applied surface tension results in the deformation of the fiber's core at the interface between the core and cladding in the longitudinal direction. This phenomenon needs to be considered for the drawn fibers, as it leads to intermodal power transfer and additional losses, which are highly dependent on the surface quality of the fiber drum, and the cabling technology used [16]. The micro-bending loss can be described by [34]

$$\alpha_{MBL} = \frac{1}{8}\left(k_0 n_{air} D_0\right)^2 \phi\left(k_0 \Delta n_{eff}\right) \text{ dB/km}, \tag{9}$$

where $k_0 = 2\pi/\lambda$ is the wavenumber of the transmitted radiation in vacuum, D_0 is the diameter of the core-guided fundamental mode LP_{01}, and Δn_{eff} is the difference between the effective refractive indices of the LP_{01} mode and the first mode with higher transverse order LP_{11}. The function $\phi\left(k_0 \Delta n_{eff}\right)$ represents the power spectral density of the micro-bending stochastic process, which is given by $\phi\left(k_0 \Delta n_{eff}\right) = C_0 / \left(k_0 \Delta n_{eff}\right)^2$ [35] with $C_0 = 1$ [34].

Figure 3 illustrates the calculated confinement losses, the surface scattering losses, the micro-bending losses, and the total losses averaged over the two orthogonally polarized fundamental modes LP_{01} of the designed straight fiber across the wavelength range from $\lambda = 400$ nm to $\lambda = 1800$ nm. The total losses, which are the sum of confinement losses, surface scattering losses, and micro-bending losses, are less than 30 dB/km, with a value of 18.1 dB/km at the wavelength of $\lambda_{op,Green} = 515$ nm and a value of 16.1 dB/km at the wavelength of $\lambda_{op,NIR} = 1030$ nm. The micro-bending and the surface scattering losses dominate in the green spectral range, while the confinement losses are the primary loss mechanism in the NIR spectral range. For the designed fiber, the wavelength of $\lambda_{op,Green} = 515$ nm is located near the center of the second transmission band, and $\lambda_{op,NIR} = 1030$ nm lies within the low-loss region of the first transmission band. This confirms the feasibility of

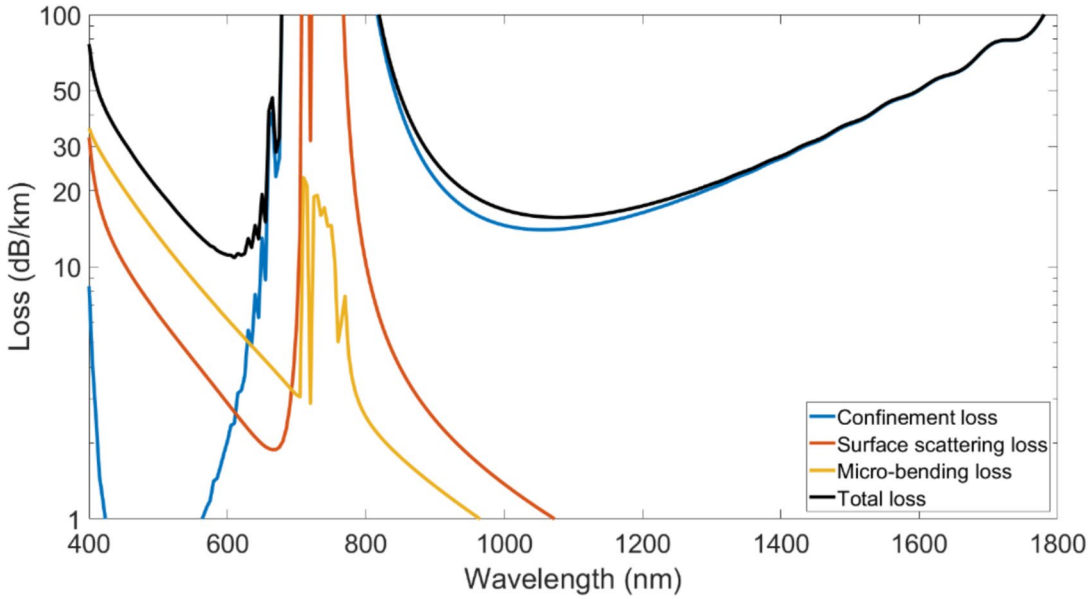

Fig. 3 Calculated confinement losses, surface scattering losses, micro-bending losses, and total losses of the fundamental mode LP_{01} of the designed straight fiber as a function of the wavelength. $\lambda_{op,Green} = 515$ nm is close the center of the second transmission band, while $\lambda_{op,NIR} = 1030$ nm lies in the first transmission band of the designed tubular IC-HCPCF

an IC-HCPCF that is capable to simultaneously guide laser radiation in both spectral ranges with low losses.

The bending behavior of the designed fiber was thoroughly analyzed by adjusting the refractive index of the fiber structure using conformal mapping [36]. Figure 4a and b present the computed confinement losses, surface scattering losses, micro-bending losses, and the total losses averaged over the two orthogonally polarized fundamental modes LP_{01} of the designed fiber for bend radii ranging from 0.2 to 0.5 m at the wavelengths of $\lambda_{op,Green} = 515$ nm and $\lambda_{op,NIR} = 1030$ nm. Despite bending, the core-guided fundamental mode LP_{01} experiences low losses at both wavelengths. The total loss amounts to only 26.6 dB/km at $\lambda_{op,Green} = 515$ nm and 19.5 dB/km at $\lambda_{op,NIR} = 1030$ nm even if the fiber is bent at a tight radius of 0.2 m.

To experimentally validate our fiber design, we fabricated the fiber using the well-known stack-and-draw technique. The results of the experimental characterization are discussed in the following section.

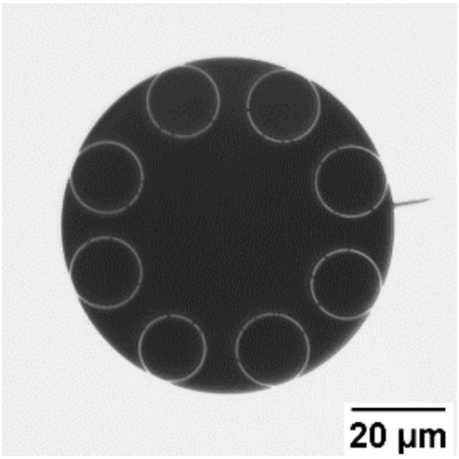

Fig. 5 Microscope image of the fabricated tubular IC-HCPCF

3 Experimental results

A fiber with a total length of approximately 300 meters was drawn using our drawing facility. Figure 5 shows the cross-sectional microscopy image of the fabricated tubular IC-HCPCF. The diameter of the hollow air core was measured to be $40.03 \pm 0.26\ \mu m$. The core of the fiber is surrounded by 8 glass capillaries. These capillaries have outer diameters ranging from $14.01 \pm 0.36\ \mu m$ to $15.35 \pm 0.34\ \mu m$ with an average outer diameter of $14.94 \pm 0.32\ \mu m$. The average thickness of the thin glass struts is 352 nm ± 25 nm, which is slightly thinner than the designed value of 362 nm. The relative deviation of the glass capillaries was about 8%, which is defined as $(d_{max} - d_{min})/d_{ave}$ where d_{max}, d_{min}, and d_{ave} are the largest, the smallest, and the average value of the outer diameters of the glass capillaries, respectively. A difference between the diameters of the capillaries in the fiber's structure, from one side to the other, is often observed in produced fibers [37]. It was shown that this asymmetry of the diameters of the capillaries is due to a higher temperature toward the one side of the preform, leading to a difference in viscosity across the cross section of the preform during drawing and causing larger diameters of the glass capillaries on the one side of the fiber than the other [38]. The outer diameter of the fiber is $281 \pm 2\ \mu m$.

The total losses of the fiber at a bend radius of 0.5 m were measured by using the cut-back method [39]. To measure the losses in the NIR spectral range, a

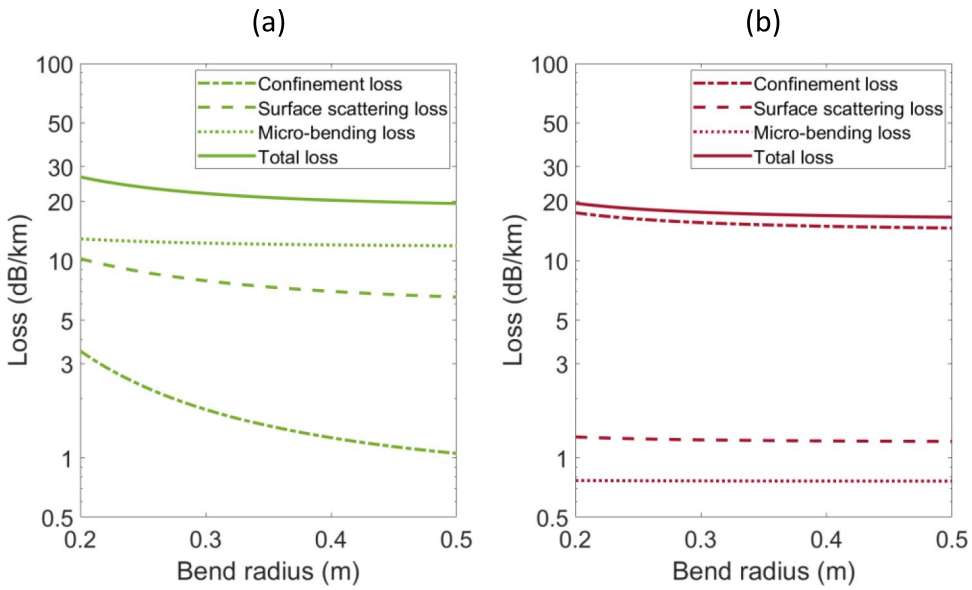

Fig. 4 Calculated bending-induced increase of the confinement losses, surface scattering losses, micro-bending losses, and total losses of the designed tubular IC-HCPCF for bend radii ranging from 0.2 to 0.5 m at the wavelength of **a** $\lambda_{op,Green} = 515$ nm, and **b** $\lambda_{op,NIR} = 1030$ nm

supercontinuum light source (NKT Photonics, SuperK COMPACT,450 – 2400 nm) was coupled to the fiber under test, which was coiled on a spool with a 0.5 m radius. The transmitted spectral power density S_{long} was measured after the long fiber piece with a length of $L_{long} = 167$ m using an optical spectrum analyzer (Anritsu, MS9710B,650 – 1800 nm). The fiber was then cut back to a shorter length of $L_{short} = 5$ m without changing the launching conditions, and the transmitted spectral power density S_{short} was measured again. The same procedure with the piece of the fiber cut off during the previous measurement was used to measure the losses in the green spectral range applying a white fiber-coupled LED (Thorlabs, MWWHF2,400 – 800 nm) as the light source. The transmitted spectral power densities S_{long} and S_{short} were measured using a spectrometer (Ocean Optics, HR 4000,200 – 1100 nm) for fiber lengths of $L_{long} = 162$ m and$L_{short} = 5$ m, respectively. The measured total losses of the fiber can be calculated using.

$$\alpha = \frac{10}{L_{long} - L_{short}} \log_{10}\left(\frac{S_{short}}{S_{long}}\right) \text{dB}. \tag{10}$$

Figure 6 compares the computed total losses of the drawn fiber at a bend radius of 0.5 m, which includes the confinement losses (which can be assumed to be only slightly increased by bending due to the comparably large bending radius), surface scattering losses, and micro-bending losses with the measured losses of the produced fiber. The measured losses were averaged over three measurements with new cleaves of the fiber end for each measurement without significantly changing the fiber length.

The calculated total losses show a good agreement with the measured losses in the NIR spectral range. We attribute the discrepancy in the loss spectra between the numerical calculation and the measurement in the green spectral range to the nonuniformity of the cladding structure along the fiber [40].

A broad transmission bandwidth of 460 nm in the NIR spectral range was identified, with measured losses of less than 50 dB/km ranging from $\lambda \approx 885$ nm to $\lambda \approx 1350$ nm. At the operation wavelength of $\lambda_{op,NIR} = 1030$ nm the measured total loss was 25.7 ± 0.7 dB/km. The second transmission band of the fiber spanned from $\lambda \approx 435$ nm to $\lambda \approx 612$ nm with measured total losses of less than 50 dB/km. The measured loss at the operation wavelength of $\lambda_{op,Green} = 515$ nm was 27.5 ± 0.3 dB/km, thus, comparable with the state-of-the-art tubular IC-HCPCFs. This corresponds to a transmission of 94.3% at $\lambda_{op,NIR} = 1030$ nm, and of 93.9% at $\lambda_{op,Green} = 515$ nm through a 10 m long fiber.

A frequency-doubled solid-state laser emitting at $\lambda_{op,Green} = 515$ nm and a broadband amplified spontaneous emission (ASE) light source with a spectrum ranging from $\lambda = 1020$ nm to $\lambda = 1080$ nm were used for an additional measurement of the total losses at a bend radius of 0.2 m. In this measurement, the measured total losses α at a bend radius of 0.5 m (see Fig. 6) were considered as the reference of the straight fiber, due to the minor influence of the bending on the total losses at such a large bend radius. A 10 m long fiber was first loosely coiled with a bend radius (BR) = 0.5 m and the transmitted power P_{ref} measured as the reference. By comparing this to the transmitted power $P_{BR=0.2\text{ m}}$ measured when the fiber was bent to a radius of 0.2 m, the total losses at the corresponding bend radius $\alpha_{BR=0.2\text{ m}}$ consisting of the sum of the bending-induced increase of the confinement losses and the measured total losses α of the fiber without bending was determined by using [41]

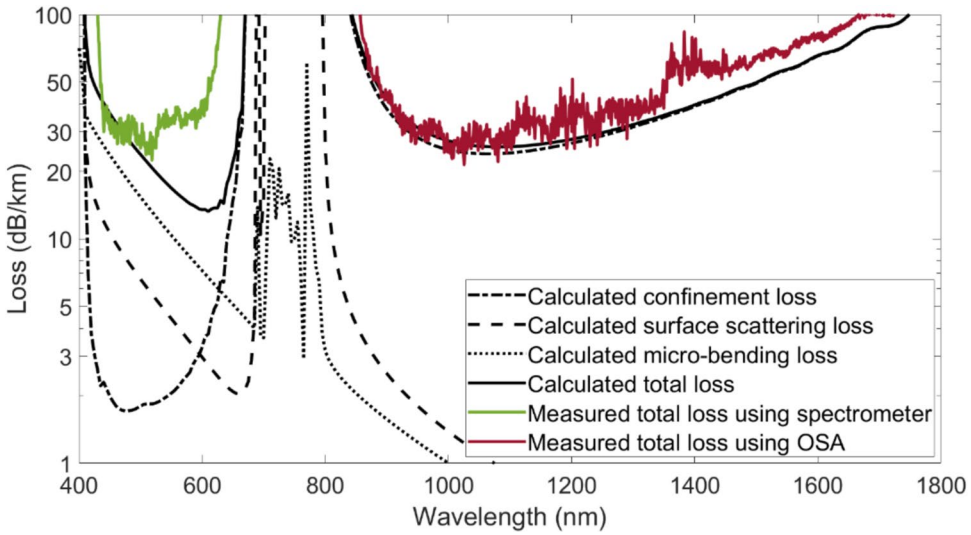

Fig. 6 Comparison between the computed total losses including the confinement losses, the surface scattering losses as well as the micro-bending losses to the measured losses of the fabricated fiber coiled with a bend radius of 0.5 m

$$\alpha_{BR=0.2\text{ m}} = \frac{10}{n2\pi R}\log_{10}\left(\frac{P_{ref}}{P_{BR=0.2\text{ m}}}\right) + \alpha\text{dB}, \tag{11}$$

where $R = 0.2$ m is the bend radius of the fiber and $n = 8$ denotes the number of turns applied during bending. Figure 7 presents a comparison between the measured total losses and the calculated total losses of the fiber at a bend radius of 0.2 m, considering the confinement losses, the surface scattering losses as well as the micro-bending losses. The calculated results agree well with the measured total losses of 34.8 ± 1.3 dB/km at $\lambda_{op,Green} = 515$ nm and 31.8 ± 0.7 dB/km at $\lambda_{op,NIR} = 1030$ nm. Compared to the measured total losses at the bend radius of $0.5m$, the increased losses of about 7.3 dB/km at $\lambda_{op,Green} = 515$ nm and about 6.1 dB/km at $\lambda_{op,NIR} = 1030$ nm affirm the minimal bending-induced increase of the confinement losses at a bend radius of 0.2 m. Specifically, this translated to a transmission of 92.9% at $\lambda_{op,NIR} = 1030$ nm, and 92.3% at $\lambda_{op,Green} = 515$ nm through a 10 m long fiber.

To analyze the beam exiting the fiber in the NIR spectral range in detail, the light of the ASE source was launched into a 10 m long piece of the fiber using a focusing lens with a focal length of $f = 50$ mm to match the diameter of the incident Gaussian beam to the calculated mode field diameter (MFD) of the fundamental mode LP_{01} of the fiber. Throughout the measurement, the fiber was loosely coiled on the optical table with a BR > 0.3 m. Figure 8 shows the measured near field (a) and far field (b) intensity distributions

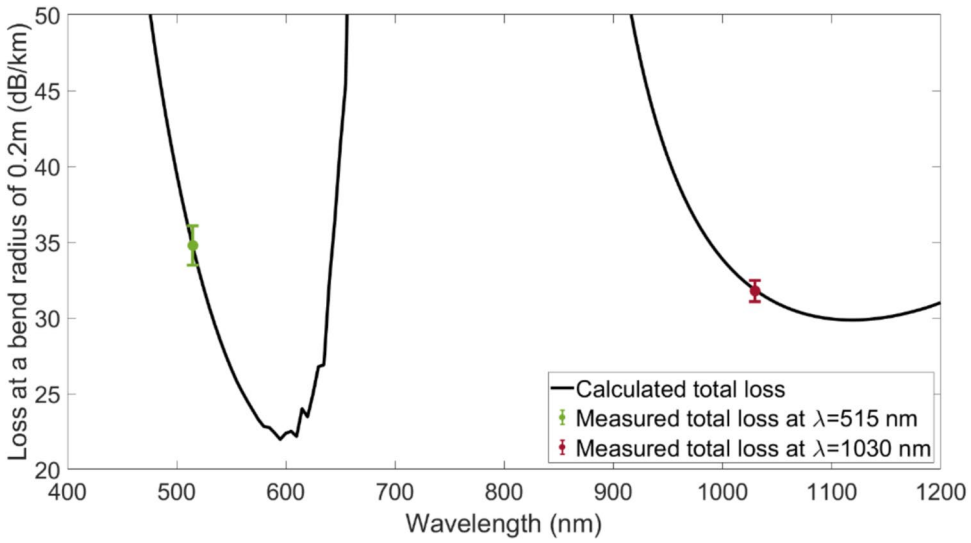

Fig. 7 Comparison between the calculated total losses including the confinement losses, the surface scattering losses as well as the micro-bending losses, and the measured total losses of the fabricated fiber at a bend radius of 0.2 m

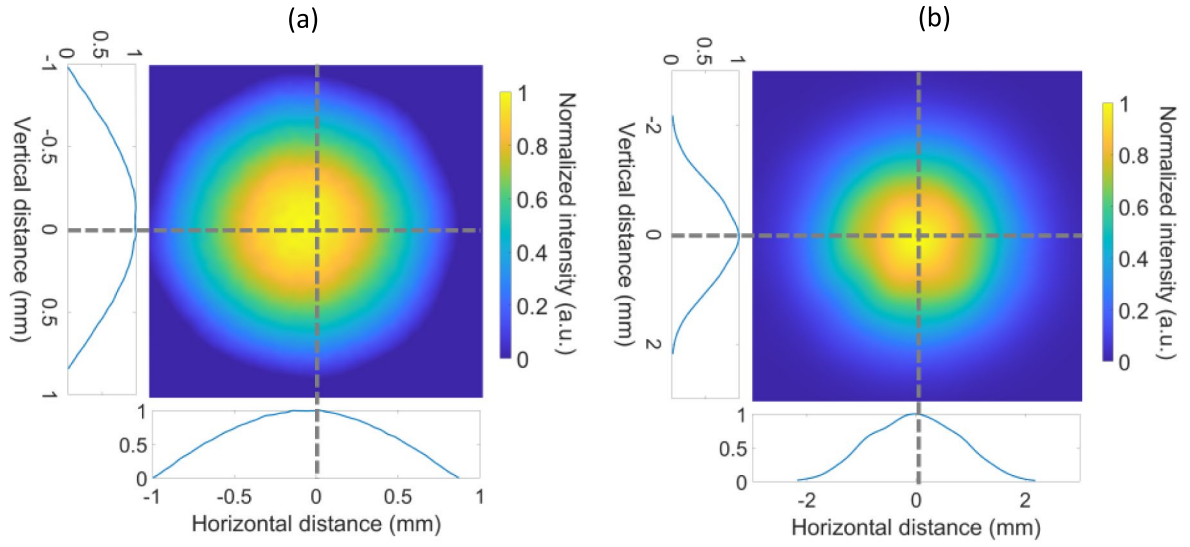

Fig. 8 Near field (**a**) and far field (**b**) intensity distributions (including the profiles measured along the dashed lines) after a 10 m long fiber at the wavelength of $\lambda_{op,NIR} = 1030$ nm as measured using an uEye camera

captured using an uEye camera for the beam transmitted through the 10 m long fiber. The beam exiting the fiber in the near field was imaged on an uEye camera using a home-built telescope with a magnification of 39.5×. The MFD was measured to be 29.61 ± 0.12 μm using the second-moment ($d4\sigma$) method [7]. The intensity distribution in the far field of the beam exiting the fiber was recorded using an uEye camera placed at the focal plane of a lens with a focal length of $f = 100$ mm. In the far field, a Gaussian-like beam profile was observed, with a measured half divergence angle of 24.17 ± 0.13 mrad.

Figure 9 shows the measured beam caustic of the refocused laser beam exiting the 10 m long fiber. The beam exiting the fiber was collimated using a lens with a focal length of $f = 30$ mm. To measure the beam propagation factor M^2, the collimated beam was refocused by a focusing lens with $f = 600$ mm inside the beam profiler (BeamSquared from Ophir Optronics Solutions). The roundness of the output beam exceeded 98%. The beam propagation factor M^2 averaged over the horizontal (X) and vertical (Y) planes was 1.09, indicating the near to diffraction-limited beam quality in the NIR spectral range. The insets in the figure show the measured intensity distributions in the focus and far field planes.

The near to diffraction-limited beam quality of the beam exiting the fiber was also confirmed by the spectrally and spatially resolved S^2 analysis, which spatially resolves the spectral interference from multiple fiber modes propagating at different group velocities [42]. Performing a Fast Fourier Transform (FFT) on the measured optical spectrum of the beam exiting the fiber allows determining the group delay difference (GDD) between the modes with higher transverse order with respect to the fundamental mode LP_{01}, thereby resolving the modal content of the beam exiting the fiber [42]. The results of this analysis are shown in Fig. 10. The plot shows the sum of the Fast Fourier transforms (FFTs) of all the optical spectra measured at each spatial position by scanning across the cross-section of the laser beam transmitted through the 10 m long fiber as a function of the measured GDD of the modes with higher transverse order with respect to the fundamental mode LP_{01}. The insets within the figure illustrate the measured intensity profiles of the fundamental mode LP_{01} (very left) and the modes with higher transverse orders. Only two LP_{11} modes were identifiable. The power ratio between the mode with higher transverse order and the fundamental mode LP_{01} was determined using the calculated multipath interference (MPI) [42]. All measured MPI values were smaller than −25 dB, indicating less than 0.3% of the optical power compared to the fundamental mode LP_{01}.

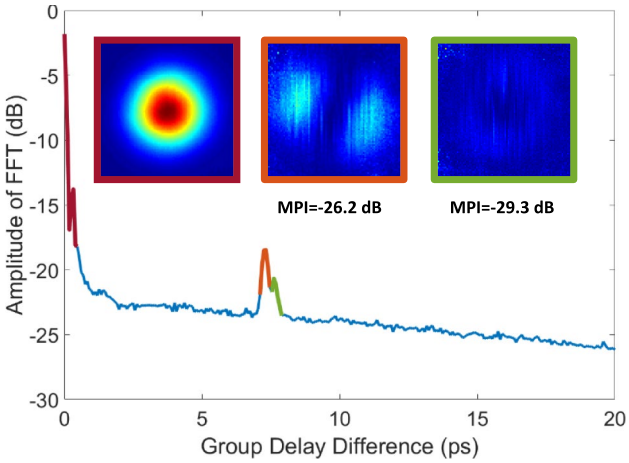

Fig. 10 Spectrally and spatially resolved S^2 analysis of the laser beam exiting the 10 m long fiber in the NIR spectral range. The insets show the measured intensity distributions of the fundamental mode LP_{01} (very left) and the modes with higher transverse order. The calculated multipath interference (MPI) corresponds to the power ratio between the mode with higher transverse order and the fundamental mode LP_{01}

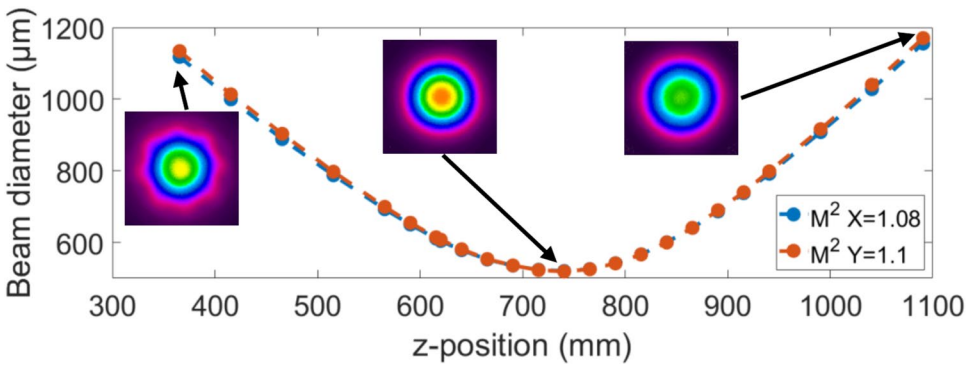

Fig. 9 Measured beam caustic of the refocused beam exiting the 10 m long fiber in the horizontal (X) and vertical (Y) planes at the wavelength of $\lambda_{op,NIR} = 1030$ nm. The beam exiting the fiber was collimated using a lens with a focal length of $f = 30$ mm. To measure the beam propagation factor M^2, the collimated beam was refocused by a lens with a focal length of $f = 600$ mm inside the beam profiler. The insets show the intensity distributions in the near and far field planes

For the analysis of the beam exiting the fiber at the wavelength of $\lambda_{op,Green} = 515$ nm, the frequency-doubled solid-state laser beam was injected into the 10 m long fiber. Due to the smaller collimated beam diameter of approximately 1.2 mm compared to 2.4 mm in the NIR spectral range before entering the fiber, the same focusing lens with a focal length of $f = 50$ mm was used to match the MFD of the fiber at this wavelength. The measured caustic of the refocused beam exiting the 10 m long fiber is shown in Fig. 11. The measured average beam propagation factor M^2 in the horizontal (X) and vertical (Y) planes was 1.14, again confirming the near-diffraction-limited beam quality also in the green spectral range.

The result of the S^2 analysis depicted in Fig. 12 reveals the modal contents of the beam exiting the fiber with the presence of the two higher-order transverse modes LP_{11} and LP_{02}. The measured MPI for these modes was −17.7 dB and −18 dB, respectively, corresponding to less than 1.7% of the power compared to the fundamental mode LP_{01}. The low power ratio between the mode with higher transverse order and the fundamental mode LP_{01} in both spectral ranges ensures good focusability of the laser beams exiting the fiber.

To illustrate the good beam quality after the transport fiber, the recorded intensity distributions in the near field and far field are shown in Fig. 13a and b, respectively. The MFD was measured to be 31.87 ± 0.21 μm, which is comparable to the MFD in the NIR spectral range. The measured far field divergence half-angle was 11.73 ± 0.23 mrad. This was approximately half of the one observed in the NIR. The measured MFDs of the beam exiting the fiber were in good agreement with the numerical calculations, which yielded 30.22 μm at $\lambda_{op,Green} = 515$ nm and 30.58 μm at $\lambda_{op,NIR} = 1030$ nm.

It was shown that achieving effective single-modeness in a straight fiber requires a ratio d_{cap}/D_{core} of approximately 0.68 [29]. This results from the mode coupling between the undesired core-guided higher order transverse mode LP_{11} and the fundamental mode in the cladding capillaries of the fiber [29]. For the designed fiber with a d_{cap}/D_{core} of 0.375, this mode coupling cannot occur. However, effective single-modeness can still be achieved under optimal launching conditions and is independent of the bend radii. Figure 14a and b show the measured beam propagation factor M^2 averaged over the horizontal (X) and vertical (Y) planes as function of bend radius at $\lambda_{op,Green} = 515$ nm and $\lambda_{op,NIR} = 1030$ nm, respectively. The insets show the corresponding intensity distributions in the far field planes of the beam exiting the 10 m long fiber.

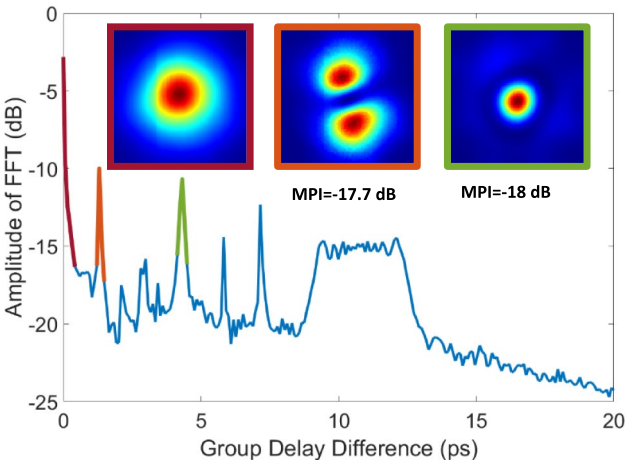

Fig. 12 Spectrally and spatially resolved S^2 analysis of the laser beam after propagating through the 10 m long fiber in the green spectral range. The insets show the measured intensity distributions of the fundamental mode LP_{01} (very left) and the modes with higher transverse order. The calculated multipath interference (MPI) corresponds to the power ratio between the mode with higher transverse order and the fundamental mode LP_{01}

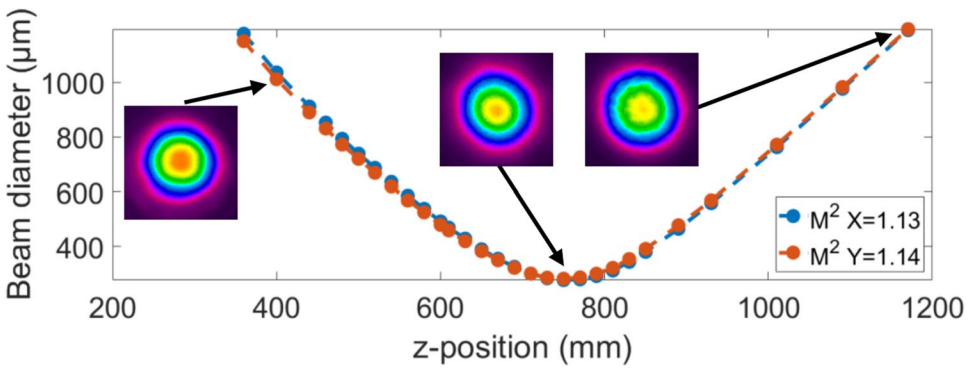

Fig. 11 Measured beam caustic of the refocused beam exiting the 10 m long fiber in the horizontal (X) and vertical (Y) planes at a wavelength of $\lambda_{op,Green} = 515$ nm. The beam exiting the fiber was collimated using a lens with a focal length of $f = 30$ mm. To measure the beam propagation factor M^2, the collimated beam was refocused by a focusing lens with $f = 600$ mm inside the beam profiler. The insets show the intensity distributions in the near and far field planes

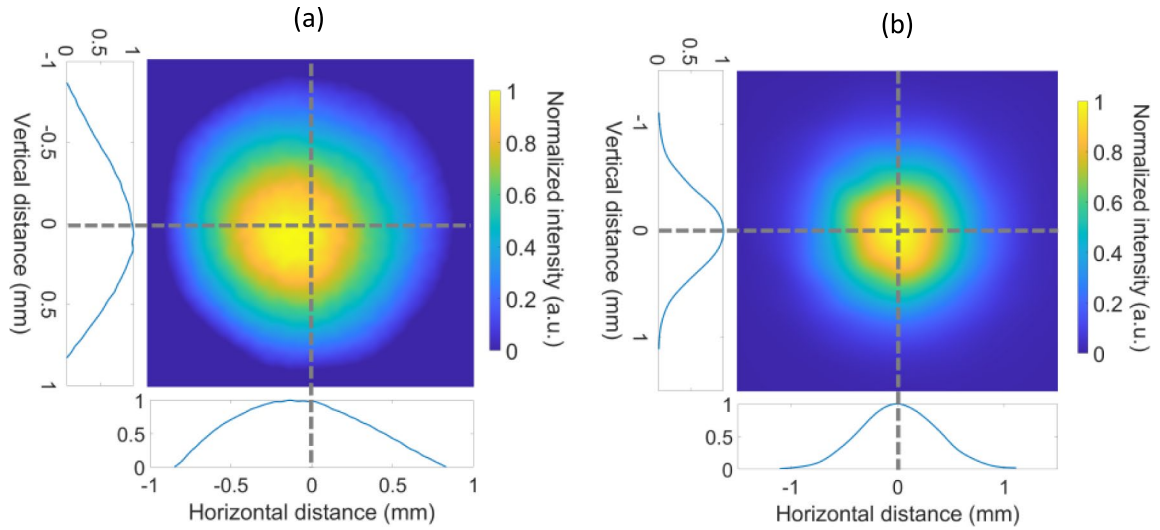

Fig. 13 Near field (**a**) and far field (**b**) intensity distributions after a 10 m long fiber at the wavelength of $\lambda_{op,Green} = 515$ nm measured using an uEye camera

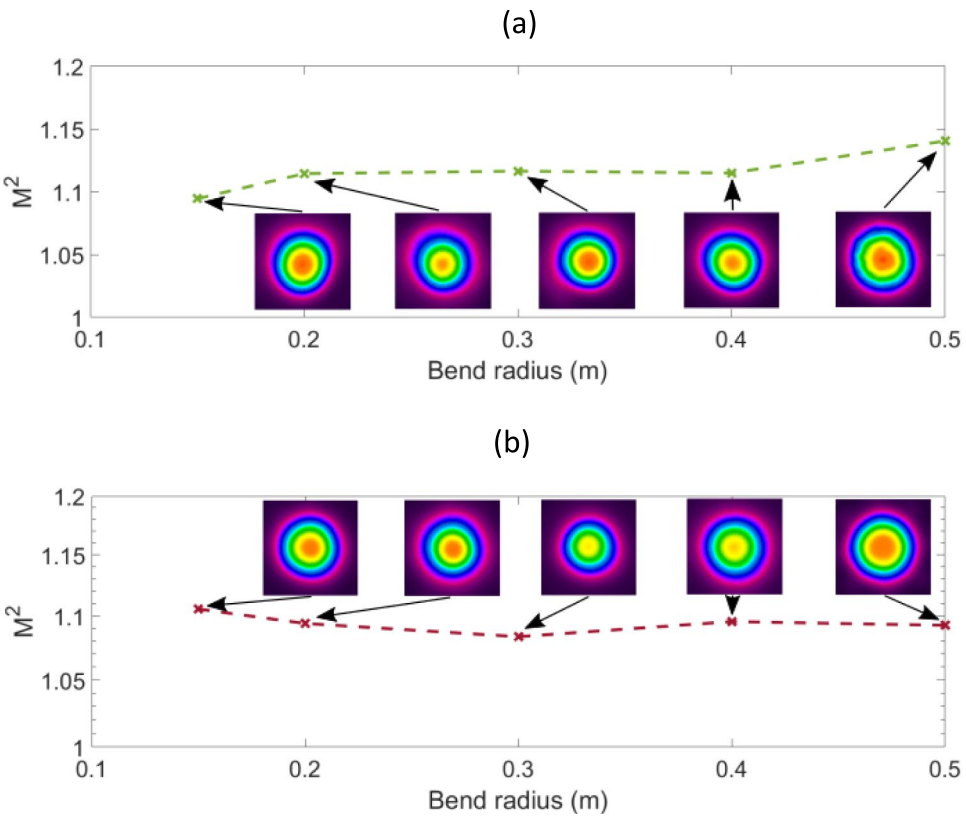

Fig. 14 Measured beam propagation factor M^2 averaged over the horizontal (X) and vertical (Y) planes as function of bend radius at the wavelength of **a** $\lambda_{op,Green} = 515$ nm, and **b** $\lambda_{op,NIR} = 1030$ nm. The insets show the corresponding intensity distributions in the far field planes of the beam exiting the 10 m long fiber

According to the numerical calculations, the chromatic dispersion of the fiber is approximately 1.02 ps/(nm · km) at $\lambda_{op,NIR} = 1030$ nm. At $\lambda_{op,Green} = 515$ nm, this value amounts to about 0.62ps/(nm · km). The low chromatic dispersion exhibited by the fiber at both operational wavelengths ensures the guiding of ultrashort laser pulses with minimal temporal distortion. The fiber's large core diameter of 40 μm for operation in the green spectral range results in a reduced power-weighted spatial overlap between the core-guided laser beam and the surrounding glass cladding compared to the core diameters of the state-of-the-art IC-HCPCFs typically in the order of 30 μm [18, 20, 21]. The

simulation shows that the power-weighted spatial overlap at $\lambda_{op,Green} = 515$ nm is about 2.9×10^{-6}. It amounts to about 1.3×10^{-5} at $\lambda_{op,NIR} = 1030$ nm. According to the theoretical analysis in ref. [43], the maximum energy of ultrashort laser pulses that can be launched into the fiber without damage is inversely proportional to this power-weighted spatial overlap. Therefore, the numerically calculated low chromatic dispersion and the low power-weighted spatial overlap suggest the potential for flexible guiding of ultrashort laser pulses at both $\lambda = 1030$ nm and $\lambda = 515$ nm using a single fiber, which will be the focus of our future work. This capability enhances the flexibility for wavelength adjustments in laser material processing applications. Combining green and NIR ultrashort laser pulses is ideal for applications like internal structuring in glass, where green pulses efficiently ablate the surface, while NIR pulses enable subsurface modifications. The high precision of green laser pulses, together with the deeper penetration of NIR laser pulses enables the fabrication of multilayer electronic devices [44]. Moreover, hybrid processes using green and NIR pulses provide benefits in laser welding of dissimilar materials [45], and surface functionalization of anti-reflective or hydrophobic surfaces [46].

The present work explores the possibility of flexible delivery of ultrashort laser pulses at $\lambda = 1030$ nm, and its second harmonic at $\lambda = 515$ nm using a single fiber with low losses. A core diameter of 40 μm was chosen as a compromise to balance optical performance across both spectral ranges. Compared to typical IC-HCPCFs designed for the NIR spectral range, which have core diameters about 60 µm, the presented fiber is more susceptible to damage at the input facet when guiding ultrashort laser pulses at $\lambda = 1030$ nm. However, previous studies have theoretically and experimentally shown that for a 10 m long vacuumized HC-NANF with a core diameter of 28.3 μm, ultrashort laser pulses with energies of up to 200 μJ and pulse durations of 40*fs* can be delivered without damaging the fiber, corresponding to a peak power of about 5 GW at $\lambda = 800$ nm [31]. The pulse duration of ultrashort laser pulses used in material processing is typically about 500*fs*. Using the same theoretical analysis, ultrashort laser pulses with a pulse energy exceeding 700 μJ and a pulse duration of 500*fs* can be launched into the presented fiber without causing damage at the fiber facet at $\lambda = 1030$ nm, corresponding to a peak power of about 1.4 GW. Considering the LIDT of silica glass for the same pulse duration at $\lambda = 515$ nm of about 2.5 J/cm^2 [47], the maximum pulse energy that can be launched into the fiber without causing damage is approximately 450 μJ, corresponding to a peak power of about 0.9 GW. According to these theoretical and experimental [31] analyses, the transmitted ultrashort laser pulses are already sufficient for applications in laser material processing such as drilling of micro-holes with high precision, functionalizing material surfaces, and processing transparent materials. Future work will focus on determining the maximum pulse energy that can be injected into the fiber without causing damage at both $\lambda = 515$ nm and $\lambda = 1030$ nm. Additionally, the long-term stability and the impact of fiber bending on the delivery of ultrashort laser pulses will be investigated. Following successful experimental studies, practical laser material processing will be demonstrated.

4 Conclusion

In summary, we presented the design, fabrication, and characterization of an 8-tube inhibited-coupling guiding hollow-core photonic crystal fiber (IC-HCPCF) capable of guiding both the beam emitted from an Yb:YAG laser at the fundamental wavelength of $\lambda = 1030$ nm and its second harmonic at $\lambda = 515$ nm. By optimizing the outer diameter of the glass capillaries, optimal performance to mitigate the bending-induced increase of the confinement loss at $\lambda = 515$ nm was possible without compromising the optical performance at $\lambda = 1030$ nm. Controlling the strut thickness of the glass capillaries to approximately 362 nm enabled dual-wavelength transmission with low losses. Experimental results showed the near to diffraction-limited beam quality with M^2<1.15 of the beam exiting the 10 m long fiber at both operational wavelengths. The measured losses of 27.5 ± 0.3 dB/km at the wavelength of 515 nm and 25.7 ± 0.7 dB/km at 1030 nm confirmed the potential of the proposed approach for flexible, low-loss guiding of ultrashort laser pulses at the two wavelengths using a single fiber. This capability enhances the flexibility for wavelength adjustments in laser material processing applications and paves the way for new hybrid processes combining green and NIR laser radiations.

Acknowledgements This work was supported by the Landesministerium für Wissenschaft, Forschung und Kunst Baden-Württemberg (Ministry of Science, Research and the Arts of the State of Baden-Wurttemberg) within the Nachhaltigkeitsförderung (sustainability support) of the projects of the Exzellenzinitiative II.

Author contributions BC conducted the theoretical and experimental investigations and wrote the manuscript. TK and GK participated in the theoretical and experimental investigations. TG and MAA assisted in the preparation of the manuscript. All authors reviewed the manuscript.

Funding Open Access funding enabled and organized by Projekt DEAL.

Data availability The data that support the findings of this study are available from the corresponding author, B. Chen, upon reasonable request.

Declarations

Conflict of interest The authors declare no competing interests.

References

1. D.J. Förster, R. Weber, D. Holder, T. Graf, Estimation of the depth limit for percussion drilling with picosecond laser pulses. Opt. Express **26**, 11546–11552 (2018). https://doi.org/10.1364/OE.26.011546
2. A.F. Lasagni, C. Gachot, K.E. Trinh, M. Hans, A. Rosenkranz, T. Roch, S. Eckhardt, T. Kunze, M. Bieda, D. Günther, V. Lang, F. Mücklich, Direct laser interference patterning, 20 years of development: from the basics to industrial applications, in *Laser-Based Micro- and Nanoprocessing XI*. (SPIE, 2017), p.1009211
3. D. Holder, M. Buser, A. Leis, R. Weber, T. Graf, Post-processing of additively manufactured metal parts by ultrashort laser pulses for high-quality net shape geometries and advanced functionality. IOP Conf. Ser. Mater. Sci. Eng. **1135**, 12005 (2021). https://doi.org/10.1088/1757-899X/1135/1/012005
4. S. Döring, S. Richter, A. Tünnermann, S. Nolte, In-situ observation of ultrashort pulse deep drilling in silicon at 1030 nm and 515 nm. In: CLEO/Europe and EQEC 2011 Conference Digest (Optica Publishing Group, 2011), p. CM_P17
5. M. Kraus, S. Collmer, S. Sommer, F. Dausinger, microdrilling in steel with frequency-doubled ultrashort pulsed laser radiation. J. Laser Micro Nanoeng. (2008). https://doi.org/10.2961/jlmn.2008.03.0001
6. S. Engler, R. Ramsayer, R. Poprawe, Process studies on laser welding of copper with brilliant green and infrared lasers. Phys. Procedia **12**, 339–346 (2011). https://doi.org/10.1016/j.phpro.2011.03.142
7. H. Hügel, T. Graf, *Materialbearbeitung mit laser: Grundlagen und Verfahren*, 5th edn. (Springer Vieweg Wiesbaden, 2023)
8. S. D'Arcangelo, L. Caprio, D. Chesi, D. Nocciolini, R. Corbinelli, B. Previtali, A.G. Demir, Comprehensive benchmarking of laser welding technologies including novel beam shapes and wavelengths for e-drive copper hairpins. Opt. Laser Technol. **169**, 109964 (2024). https://doi.org/10.1016/j.optlastec.2023.109964
9. A. Lemke, D. Ashkenasi, H.J. Eichler, Picosecond laser induced selective removal of functional layers on CIGS thin film solar cells. Phys. Procedia **41**, 769–775 (2013). https://doi.org/10.1016/j.phpro.2013.03.146
10. S. Grabmann, L. Tomcic, M.F. Zaeh, Laser beam welding of copper foil stacks using a green high power disk laser. Procedia CIRP **94**, 582–586 (2020). https://doi.org/10.1016/j.procir.2020.09.080
11. H. Sakr, T.D. Bradley, G.T. Jasion, E.N. Fokoua, S.R. Sandoghchi, I.A. Davidson, A. Taranta, G. Guerra, W. Shere, Y. Chen, J.R. Hayes, D.J. Richardson, F. Poletti, Hollow core NANFs with five nested tubes and record low loss at 850, 1060, 1300 and 1625nm. In: Optical Fiber Communication Conference (OFC) 2021 (Optica Publishing Group, 2021), p. F3A.4
12. L. Rosa, F. Melli, L. Vincetti, Analytical formulas for dispersion and effective area in hollow-core tube lattice fibers. Fibers (2021). https://doi.org/10.3390/fib9100058
13. S. Gu, X. Wang, H. Jia, Z. Lian, X. Shen, Y. Mai, S. Lou, Single-ring hollow-core anti-resonant fiber with a record low loss (4.3|dB/km) for high-power laser delivery at 1|μm. Opt. Lett. **47**, 5925–5928 (2022). https://doi.org/10.1364/OL.467557
14. B. Debord, F. Amrani, L. Vincetti, F. Gérôme, F. Benabid, Hollow-core fiber technology: the rising of "gas photonics." Fibers (2019). https://doi.org/10.3390/fib7020016
15. B. Debord, M. Alharbi, T. Bradley, C. Fourcade-Dutin, Y.Y. Wang, L. Vincetti, F. Gérôme, F. Benabid, Hypocycloid-shaped hollow-core photonic crystal fiber part I: arc curvature effect on confinement loss. Opt. Express **21**, 28597–28608 (2013). https://doi.org/10.1364/OE.21.028597
16. E.N. Fokoua, S.A. Mousavi, G.T. Jasion, D.J. Richardson, F. Poletti, Loss in hollow-core optical fibers: mechanisms, scaling rules, and limits. Adv. Opt. Photonics **15**, 1–85 (2023). https://doi.org/10.1364/AOP.470592
17. M. Maurel, M. Chafer, A. Amsanpally, M. Adnan, F. Amrani, B. Debord, L. Vincetti, F. Gérôme, F. Benabid, Optimized inhibited-coupling kagome fibers at Yb–Nd: Yag (8.5 dB/km) and Ti: Sa (30 dB/km) ranges. Opt. Lett. **43**, 1598–1601 (2018). https://doi.org/10.1364/OL.43.001598
18. J.H. Osório, F. Amrani, F. Delahaye, A. Dhaybi, K. Vasko, F. Melli, F. Giovanardi, D. Vandembroucq, G. Tessier, L. Vincetti, B. Debord, F. Gérôme, F. Benabid, Hollow-core fibers with reduced surface roughness and ultralow loss in the short-wavelength range. Nat. Commun.Commun. **14**, 1146 (2023). https://doi.org/10.1038/s41467-023-36785-6
19. F. Poletti, Nested antiresonant nodeless hollow core fiber. Opt. Express **22**, 23807–23828 (2014). https://doi.org/10.1364/OE.22.023807
20. B. Debord, M. Alharbi, A. Benoît, D. Ghosh, M. Dontabactouny, L. Vincetti, J.-M. Blondy, F. Gérôme, F. Benabid, Ultra low-loss hypocycloid-core kagome hollow-core photonic crystal fiber for green spectral-range applications. Opt. Lett. **39**, 6245–6248 (2014). https://doi.org/10.1364/OL.39.006245
21. S.-F. Gao, Y.-Y. Wang, X.-L. Liu, C. Hong, S. Gu, P. Wang, Nodeless hollow-core fiber for the visible spectral range. Opt. Lett. **42**, 61–64 (2017). https://doi.org/10.1364/OL.42.000061
22. M. Chafer, J.H. Osório, F. Amrani, F. Delahaye, M. Maurel, B. Debord, F. Gérôme, F. Benabid, 1-km hollow-core fiber with loss at the silica rayleigh limit in the green spectral region. IEEE Photonics Technol. Lett. **31**, 685–688 (2019). https://doi.org/10.1109/LPT.2019.2904341
23. S. Eilzer, B. Wedel, Ultrafast fiber beam delivery for green wavelengths, in *Laser-Based Micro- and Nanoprocessing XV*. (SPIE, 2021), p.1167415
24. A. Hess, R. Weber, A. Heider, T. Graf, Forced deep-penetration welding with low-power second-harmonic assistance of cw copper welding with 1 μm wavelength. Phys. Procedia **5**, 29–36 (2010). https://doi.org/10.1016/j.phpro.2010.08.026
25. M.H. Frosz, P. Roth, M.C. Günendi, P.S.J. Russell, Analytical formulation for the bend loss in single-ring hollow-core photonic crystal fibers. Photonics Res. **5**, 88–91 (2017). https://doi.org/10.1364/PRJ.5.000088
26. G. Jackson, G.T. Jasion, T.D. Bradley, F. Poletti, I.A. Davidson, Three stage HCF fabrication technique for high yield, broadband UV-visible fibers. Opt. Express **32**, 7720–7730 (2024). https://doi.org/10.1364/OE.507703
27. G.T. Jasion, J.R. Hayes, N.V. Wheeler, Y. Chen, T.D. Bradley, D.J. Richardson, F. Poletti, Fabrication of tubular anti-resonant hollow core fibers: modelling, draw dynamics and process optimization.

Opt. Express **27**, 20567–20582 (2019). https://doi.org/10.1364/OE.27.020567
28. M. Zeisberger, M.A. Schmidt, Analytic model for the complex effective index of the leaky modes of tube-type anti-resonant hollow core fibers. Sci. Rep. **7**, 11761 (2017). https://doi.org/10.1038/s41598-017-12234-5
29. P. Uebel, M.C. Günendi, M.H. Frosz, G. Ahmed, N.N. Edavalath, J.-M. Ménard, P.S.J. Russell, Broadband robustly single-mode hollow-core PCF by resonant filtering of higher-order modes. Opt. Lett. **41**, 1961–1964 (2016). https://doi.org/10.1364/OL.41.001961
30 S. Eilzer, B. Wedel, Hollow core optical fibers for industrial ultra short pulse laser beam delivery applications. Fibers (2018). https://doi.org/10.3390/fib6040080
31. A. Lekosiotis, F. Belli, C. Brahms, M. Sabbah, H. Sakr, I.A. Davidson, F. Poletti, J.C. Travers, On-target delivery of intense ultrafast laser pulses through hollow-core anti-resonant fibers. Opt. Express **31**, 30227–30238 (2023). https://doi.org/10.1364/OE.496506
32. J.-P. Berenger, A perfectly matched layer for the absorption of electromagnetic waves. J. Comput. Phys.Comput. Phys. **114**, 185–200 (1994). https://doi.org/10.1006/jcph.1994.1159
33. W.Y. Crutchfield, H. Cheng, L. Greengard, Sensitivity analysis of photonic crystal fiber. Opt. Express **12**, 4220–4226 (2004). https://doi.org/10.1364/OPEX.12.004220
34. E. Numkam Fokoua, Y. Chen, D.J. Richardson, F. Poletti, Microbending effects in hollow-core photonic bandgap fibers. In: ECOC 2016; 42nd European Conference on Optical Communication, 2016, p. 1–3
35. F. Melli, L. Rosa, L. Vincetti, Analytical formulas for micro-bending and surface scattering loss estimation in tube lattice fibers. J. Lightwave Technol. **41**, 5714–5721 (2023). https://doi.org/10.1109/JLT.2023.3265167
36. R.T. Schermer, J.H. Cole, Improved bend loss formula verified for optical fiber by simulation and experiment. IEEE J. Quantum Electron. **43**, 899–909 (2007)
37. M.B.S. Nawazuddin, N.V. Wheeler, J.R. Hayes, S.R. Sandoghchi, T.D. Bradley, G.T. Jasion, R. Slavík, D.J. Richardson, F. Poletti, Lotus-shaped negative curvature hollow core fiber with 10.5 dB/km at 1550 nm wavelength. J. Lightwave Technol. **36**, 1213–1219 (2018)
38. R. Mears, K. Harrington, W.J. Wadsworth, J.M. Stone, T.A. Birks, Multi-core anti-resonant hollow core optical fiber. Opt. Lett. **49**, 6761–6764 (2024). https://doi.org/10.1364/OL.543062
39. F. Mitschke, *Fiber Optics: Physics and Technology* (Springer, Berlin Heidelberg, 2016)
40. Q. Fu, I.A. Davidson, S.M.A. Mousavi, H.C.H. Mulvad, N.V. Wheeler, L. Xu, F. Poletti, D.J. Richardson, Hollow-core fiber: breaking the nonlinearity limits of silica fiber in long-distance green laser pulse delivery. Laser Photonics Rev. **18**, 2201027 (2024). https://doi.org/10.1002/lpor.202201027
41 M. Vogel, *Speciality Fibers for High Brightness Laser Beam Delivery* (Utz, München, 2014)
42. J.W. Nicholson, A.D. Yablon, S. Ramachandran, S. Ghalmi, Spatially and spectrally resolved imaging of modal content in large-mode-area fibers. Opt. Express **16**, 7233–7243 (2008). https://doi.org/10.1364/OE.16.007233
43. B. Beaudou, F. Gerôme, Y.Y. Wang, M. Alharbi, T.D. Bradley, G. Humbert, J.-L. Auguste, J.-M. Blondy, F. Benabid, Millijoule laser pulse delivery for spark ignition through kagome hollow-core fiber. Opt. Lett. **37**, 1430–1432 (2012). https://doi.org/10.1364/OL.37.001430
44. Q. Yang, Z. Hu, M.-H. Seo, Y. Xu, Y. Yan, Y.-H. Hsu, J. Berkovich, K. Lee, T.-L. Liu, S. McDonald, H. Nie, H. Oh, M. Wu, J.-T. Kim, S.A. Miller, Y. Jia, S. Butun, W. Bai, H. Guo, J. Choi, A. Banks, W.Z. Ray, Y. Kozorovitskiy, M.L. Becker, M.A. Pet, M.R. MacEwan, J.-K. Chang, H. Wang, Y. Huang, J.A. Rogers, High-speed, scanned laser structuring of multi-layered eco/bioresorbable materials for advanced electronic systems. Nat. Commun.Commun. **13**, 6518 (2022). https://doi.org/10.1038/s41467-022-34173-0
45. P. Stritt, C. Hagenlocher, C. Kizler, R. Weber, C. Rüttimann, T. Graf, Laser spot welding of copper-aluminum joints using a pulsed dual wavelength laser at 532 and 1064nm. Phys. Procedia **56**, 759–767 (2014). https://doi.org/10.1016/j.phpro.2014.08.083
46. S. Tasleem, A. Sabah, U.A. Cheema, A. Sabir, Transparent hydrophobic hybrid silica films by green and chemical surfactants. ACS Omega **4**, 13543–13552 (2019). https://doi.org/10.1021/acsomega.9b01894
47. D.-B.L. Douti, L. Gallais, M. Commandré, Laser-induced damage of optical thin films submitted to 343, 515, and 1030 nm multiple subpicosecond pulses. Opt. Eng. **53**, 122509 (2014). https://doi.org/10.1117/1.OE.53.12.122509